2 THE ROLE OF BOUNDARY-CROSSING IN EPITHELIAL WOUND HEALING

Abstract

The processes of wound healing and collective cell migration have been studied for decades. Intensive research has been devoted to understanding the mechanisms involved in wound healing, but the role of cell-substrate interactions is still not thoroughly understood. Here we probe the role of cell-substrate interactions by examining *in vitro* the healing of monolayers of human corneal epithelial (HCE) cells cultured on artificial extracellular matrix (aECM) proteins. We find that the rate of wound healing is dependent on the concentration of fibronectin-derived (RGD) cell-adhesion ligands in the aECM substrate. The wound closure rate varies nearly six fold on the substrates examined, despite the fact that the rate of migration of individual cells shows little sensitivity to the RGD concentration (which varies 40-fold). To explain this apparent contradiction, we study collective migration by means of a dynamic Monte-Carlo simulation. The cells in the simulation spread, retract, and proliferate with probabilities obtained from a simple phenomenological model. Results of the simulation reveal that the overall wound closure rate is determined by the probability of crossing the boundary between the matrix deposited underneath the cell sheet and the aECM protein.

Manuscript prepared for submission by Eileen Fong[1], Shelly Tzlil,[2] and David A. Tirrell[1,2]

(1) Department of Bioengineering, California Institute of Technology

(2) Division of Chemistry and Chemical Engineering, California Institute of Technology

2.1 Introduction

The collective migration of cells is fundamental to wound healing, morphogenesis and many bioengineering applications. Wound healing in particular involves the migration of cell sheets over adhesive surfaces. Two mechanisms of migration have been identified in wound healing (*1*). First is the "purse string" mechanism where a marginal actomyosin cable develops along the wound edge, and wound closure proceeds with contraction of the actin belt (*2*). The second mechanism involves active spreading and migration of cells at the wound edge, known commonly as "lamellipodial crawling". The latter mechanism is more commonly observed *in vitro* and has been characterized by using scratch-wound models. In these models, cells experience an injury, which triggers cell migration through various biochemical signaling events (*3*). It has also been argued that the availability of free space is sufficient to initiate cell migration in the absence of mechanical injury (*4-6*). Upon wounding, proliferation is up-regulated (*7*).

Adhesive cell-substratum interactions are required for sustained migration into the wound area (*8, 9*). The rates of migration of individual cells are governed by surface adhesivity in a biphasic fashion, at least under certain conditions (*10*). Surfaces modified with adhesion ligands such as fibronectin (FN) (*11, 12*) and Arg-Gly-Asp (RGD) peptides have been shown to facilitate wound healing, and it is reasonable to infer that the observed increases in healing rates arise primarily from faster migration of individual cells. We show here that other factors are more important.

The substrates used in this work were prepared from artificial extracellular matrix (aECM) proteins that combine domains derived from fibronectin and elastin (15) (Figure A1). We and others have shown that such aECM proteins can be crosslinked to yield materials with elastic moduli similar to those of natural elastins (*13-15*), and that presentation of the fibronectin-derived RGD sequence promotes cell spreading and adhesion (*16-18*).

Wound healing was examined in monolayers of human corneal epithelial cells (HCE) cultured on aECM protein substrates that present controlled, varying densities of the RGD sequence. HCE cells undergo rapid re-epithelization *in vivo (19).* Both the $\alpha_5\beta_1$ and $\alpha_v\beta_3$ integrins, which bind RGD, are up-regulated by wounding (*20*). Crosslinked films with varying RGD densities were prepared by mixing aECM proteins containing RGD and "scrambled" (RDG) domains. Substrates are identified by specifying the percentage of the RGD protein in the film (e.g., 100% RGD).

2.2 Materials and methods

Protein expression and purification

Standard methods for cloning, bacterial growth, protein expression, sodium dodecyl sulfate-polyacrylamide gel electrophoresis (SDS-PAGE), and Western blotting were used to prepare and characterize aE-RGD and aE-RDG (*16*). Typical yields of protein obtained from 10 L fermentation cultures were approximately 500 mg. The molar masses of aE-RGD and aE-RDG were 34.8 kDa.

Preparation of spin-coated aECM Films

Round glass coverslips (12 mm diameter; No. 1, Deckgläser, Germany) were sonicated in a mixture of ethanol and KOH for 15 min and rinsed several times with distilled H_2O. aECM protein solutions were prepared by dissolving mixtures of aE-RGD and aE-RDG (100 mg/ml in ddH_2O) for 3 – 4 h at 4 ºC. Protein solutions containing 2.5%, 5%, 20%, 35%, 50%, 70%, 75%, 80%, 90%, and 100% aE-RGD were prepared. Bis[sulfosuccinimidyl] suberate (BS^3) was used to crosslink the aECM protein substrates. BS^3 (2.0 mg; Pierce, Rockford, IL) was dissolved in 17 µl of sterile distilled H_2O and added to 150 µl of protein solution, mixed, and centrifuged to remove bubbles. The stoichiometric ratio of activated esters in BS^3 to primary amines in the aECM proteins was roughly 1:1. A 17 µl volume of BS^3-protein solution was then spin-coated on a 12 mm diameter round glass cover slip at 7000 rpm for 30 sec at 4 ºC. Each protein film was stored overnight at 4 ºC before use.

Generation of aECM films containing boundaries

We prepared 100 µl of aECM protein solutions (25 mg/ml in distilled H_2O) containing 0%, 2.5%, 20%, 50%, and 100% aE-RGD and BS^3 (0.29 mg in 2.5 µl ddH_2O) as previously described. The protein solution (17 µl) was spin-coated onto a 12 mm diameter round glass coverslip at 5000 rpm 30 sec at 4 °C. Protein films were allowed to dry overnight at 4 °C. Subsequently, 600 µl of aECM protein solution (15 mg/ml) was mixed with 1.725 mg of BS^3 dissolved in 12.75 µl distilled H_2O. A small volume (2 µl) of the second aECM protein solution was pipetted across the middle of the film and spin-

coated at 5000 rpm for 30 sec at 4 °C. Under these conditions, an interface was generated between two distinct surface chemistries.

Characterization of substrates by atomic force microscopy (AFM)

Images and force curves were collected on an Asylum MFP-3D-BIO atomic force microscope, with accompanying IGOR Pro v.5.05 software. Pyramidal-tipped silicon nitride cantilevers (Veeco DNP-S) with nominal spring constant 0.58 N/m were used for imaging. The tip of a pair of fine forceps was drawn lightly across the surface of the protein film, prepared as described above, tearing away the protein along the scratch and exposing the underlying glass substrate. The edge of the scratch was imaged by AFM both dry and in water, and the thickness of the film was determined. Scans were made at various positions along the scratch to obtain an average measurement. The average film thickness was calculated by averaging the height measurements obtained from 5 positions, using the revealed glass as a baseline. Thicknesses measured on three separate films were averaged.

For nanoindentation studies, tips with 600 nm SiO_2 microspheres attached at the tip end (Novascan Technologies, IA) were used (*14*). Protein films with pre-determined thicknesses were immersed in water for at least 1 h at room temperature to allow equilibrium water uptake. Both the films and the cantilever assembly were submerged in water under ambient conditions during nanoindentation. Force curves were collected; the instrument records *z* (piezo) displacement and force, the product of measured tip deflection and cantilever spring constant. The maximum indentation force was set to 50

nN relative to the contact point. The tip speed was 1 μm/sec, and data were collected at 0.5 Hz.

The spring constants of the tips used for nanoindentation were determined to be about 0.3 N/m using thermal calibration in water. The Dimitriadis model (*21*) for indentation of linear-elastic soft material films of finite height with a spherical indenter was applied to the loading force data. Only force-indentation points between 20 nm and 10% maximum indentation were used to constrain the data to the near-linear response range. The elastic modulus was obtained by averaging the calculated moduli at multiple points in three separate films.

Human corneal epithelial (HCE) cell culture

Primary human corneal epithelial cells were obtained from ScienCell Research Laboratories (San Diego, CA, #6510) and Cascade Biologics (Portland, OR, #C-019-5C). All cells were maintained in serum-free EpiLife culture medium (with 60 μM $CaCl_2$, Cascade Biologics) supplemented with Human Corneal Growth Supplement (HCGS containing bovine pituitary extract, bovine insulin, hydrocortisone, bovine transferring, and mouse epidermal growth factor, Cascade Biologics). Gentamicin (10 μg/ml) and amphotericin (0.25 μg/ml) were also added to culture media. Serum-free EpiLife medium was used in all experiments to exclude extracellular matrix proteins (i.e., fibronectin, laminin) present in serum. Cells between passages 2 to 7 were used.

Cell spreading

Aliquots (500 μl) of FN and BSA solutions were added to the wells of a transparent 24-well plate (Falcon BD, VWR, Batavia, IL) and allowed to adsorb overnight at 4 ºC. In these experiments, fibronectin (FN, 10 μg/ml in PBS, Chemicon, MA) was used as a positive control and bovine serum albumin (BSA, 2 mg/ml in PBS, Sigma) was used as a negative control. Subsequently, wells were rinsed twice with pre-warmed PBS solution and blocked with 500 μl of 0.2 wt% heat-inactivated BSA solution at room temperature for 30 min. At the same time, coverslips containing spin-coated aECM protein films were mounted in empty wells by dotting sterile grease around the circumference of the coverslips. Gentle pressure was applied to ensure firm adhesion to the well. Finally, all wells were rinsed twice with pre-warmed PBS solution.

HCE cells were enzymatically passaged using 0.05 % Trypsin-0.25 % EDTA (Cascade Biologics). To each well, 4.8×10^4 cells were added together with 1 ml of fresh EpiLife medium. The plates were swirled gently to prevent clustering of cells and placed in an incubator at 37 ºC under 5% CO_2/95 % air. Images of five random positions in each well were acquired after 4 hours. 200 cells were traced for each surface using ImageJ and their areas were recorded. Cells with projected areas above 300 μm^2 (based on the average cell areas on BSA) were considered spread and the percentage of spread cells was plotted for each surface.

Wound healing

The experimental setup was adapted from Nikolić et al. with modifications (*6*). Slabs of polydimethylsiloxane (PDMS; Dow Corning, Midland, MI) were cast to 0.3 mm thickness according to the manufacturer's instructions. Briefly, PDMS was mixed at 10:1 PDMS base/curing agent ratio, poured into a 100 mm petri dish to 0.3 mm height, degassed in a desiccator for at least 1 h and baked for at least 2 h at 65 °C. Blocks of PDMS with lateral dimensions roughly 2 mm x 2 mm were cut with a sterile scalpel, sterilized with ethanol and air-dried. Use of thin (0.3 mm) blocks of PDMS allowed cells to maintain confluence across the edge of the block and prevented contact between cells and the underlying substrate surface.

The PDMS blocks were placed at the center of the coverslips containing spin-coated aECM films. These coverslips were then subsequently mounted in 24-well tissue culture plates by using sterile vacuum grease (Dow Corning, Midland, MI). To all wells, 500 µl of FN was added overnight at 4 °C to cover the entire surface to aid cell adhesion. The next day, 2 x 10^5 primary HCE cells were seeded into each well and allowed to grow to confluence in 3 – 5 days. The medium was changed every two days. Once a confluent monolayer formed, the PDMS blocks were lifted with sterile tweezers, creating a wounded cell sheet. A schematic drawing of the experimental set up is shown in Figure 2.2A.

Each well was rinsed twice with fresh medium before the start of each experiment to remove any cell debris. Meanwhile, a chamber was set up around the microscope to maintain the microscope stage and chamber interior at 37 ºC with 5% CO_2/95% air to

sustain cells. A hole was made in the cover of one of the empty wells in the 24-well plate and the air supply was attached to ensure that cells were maintained under the CO_2/air mixture. Water was also added to surrounding empty wells to prevent excessive evaporation of the medium. Wound closure was followed for 30 h by time-lapse phase contrast microscopy on a Nikon Eclipse TE300 microscope at 10 x magnification. Digital images of at least 5 different spots of the wound edge for each substrate were acquired every 15 min using MetaMorph v6.3.2 (Molecular Devices, Sunnyvale, CA).

The wound areas immediately after wounding (t = 0 h) and after 30 h (t = 30 h) were traced manually using ImageJ v1.37 (NIH, USA, http://rsb.info.nih.gov/ij/). The difference in the two areas was then divided by the length of the wound edge to yield the distance traveled by the cell sheet. This distance was then divided by the total time (30 h) to give the wound closure rate. The overall wound closure rates were obtained by averaging the wound closure rates calculated from all the videos obtained from more than three independent experiments.

Cell tracking was performed to explain the differences in overall wound closure behaviors observed on surfaces with different RGD densities. Individual cells within the cell sheet were also tracked manually using ImageJ, with MTrackJ, a plug-in created by Meijering and colleagues at the University Medical Center Rotterdam, Netherlands (http://www.bigr.nl/). Trajectories of individual cells were tracked frame by frame for the last 10 h for each video. The average cell speed (μm/min) of an individual cell was

determined by averaging the speeds calculated in each 15 min interval. Only the cells that migrated on the test surface were included in the analysis.

The calculated cell speeds were slightly below the reported range of 60 – 80 μm/h (*19, 22*). However, these differences could be characteristic of tissue culture monolayers and the use of serum-free media.

Interface-crossing experiments

aECM surfaces containing substrate interfaces were mounted into the wells of a 24-well tissue culture plate. HCE cells (1×10^4) were added to each well and allowed to attach for 2 h at 37 °C at 5% CO_2/ 95% air. Images of the interface at several positions on the aECM film were acquired every 15 min for 24 h using phase contrast microscopy at 37 °C at 5% CO_2/ 95% air.

Time-lapse videos were analyzed using ImageJ. We tracked cells that contacted the interface and recorded the time spent at the interface before a "decision" was made (i.e., the cell crossed the interface or moved away). We considered each encounter a separate "event" (i.e., once the cell leaves the interface and re-contacts the interface again, the timing restarts). The total amount of time spent at the interface and the subsequent decision (i.e., to cross the interface or not) were recorded for at least 150 events for each condition.

Statistical analysis

For all experimental data, the statistical significance of differences was estimated by analysis of variance followed by the Tukey test. Differences were taken to be significant at $P \leq 0.05$.

2.3 Results and discussion

Dehydrated films were determined to be in the range of 192.64 ± 19.27 nm (n = 70) in thickness; hydrated films were 349.15 ± 26.27 nm (n = 36) thick. Based on measured height differences, water content in hydrated films was estimated to be approximately 45%. The elastic modulus of a hydrated film was determined to be 0.24 ± 0.06 MPa (n = 21), which falls within the range previously determined for films of similar aECM proteins (*14*). There were no discernible physical differences between aE-RDG and aE-RGD films with varying RGD concentrations.

HCE cells were allowed to spread on spin-coated aECM films containing varying RGD densities. After 4 h, HCE cells were well-spread on crosslinked 100% RGD and on adsorbed FN, but remained rounded on the scrambled control (0% RGD) and on adsorbed BSA surfaces (Figures 2.1A – D). To quantify these differences, projected areas of 250 cells were measured at each of several time points over a 4 h period. Cells with projected areas larger than 300 μm^2 were considered well-spread. The percentage of well-spread cells on aECM films increased with RGD density (Figure 2.1E). Although some cells eventually spread on the scrambled control substrate, spreading on the control surface was likely a consequence of cellular secretion of ECM proteins (*23, 24*).

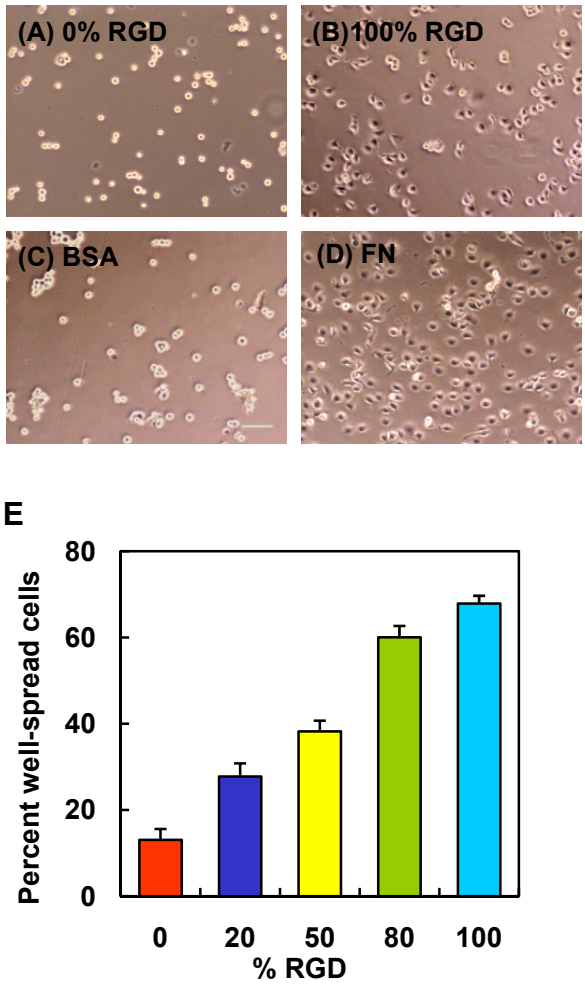

Figure 2.1 HCE cell spreading behavior on various substrates. Phase contrast images of HCE cells after 4 h on crosslinked spin-coated aECM films prepared from 0% RGD (**A**) or 100% RGD (**B**), adsorbed bovine serum albumin (BSA, **C**) and adsorbed fibronectin (FN, **D**). Scale bar = 100 μm. (**E**) Percent well-spread cells after 4 h on spin-coated aECM films with varying RGD densities. Error bars represent SEM.

Conventional scratch wound assays are limited by interference from proteins deposited by cells removed from the wound. Recent work of Nikolić et al. (*6*) and others (*25*) showed that removal of a PDMS barrier triggered cell responses similar to those

observed in scratch wound assays. Using a similar approach, we pre-coated glass coverslips with the protein of interest and laid down a short PDMS slab to provide a temporary platform for cell attachment. To facilitate cell attachment, fibronectin was incubated in each well overnight prior to plating of HCE cells (Figure 2.2A). Removal of the PDMS slab placed the edge of the wounded cell sheet in contact with the test surface.

HCE cells migrated collectively in the direction of the wound by lamellipodial crawling on 100% RGD, consistent with previous reports (*5, 26*). On 2.5% RGD, however, minimal advance of the cell sheet was observed, even though cells at the wound edge were constantly extending protrusions (Figure 2.2B). Figure 2.3A shows the average displacement of the cell sheet on various surfaces as a function of time. The overall wound closure rate increases approximately 5.6-fold as the RGD density increases (Figure 2.3B and Table A1). Individual cells within the cell sheet were also tracked for the last 10 h of each video (Figure 2.3C). Cells were selected at random and only cells that migrated on the test surface were included in the analysis. Surprisingly, the cells did not migrate significantly faster on 100% RGD than on 2.5% RGD.

A

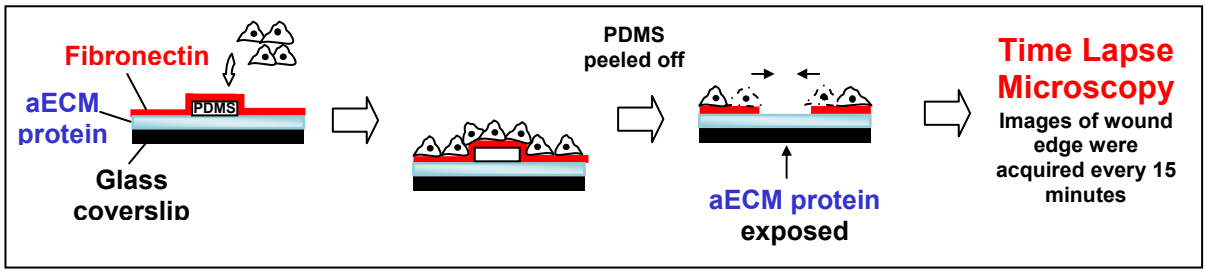
Fibronectin
aECM protein
PDMS
Glass coverslip
PDMS peeled off
aECM protein exposed
Time Lapse Microscopy
Images of wound edge were acquired every 15 minutes

B

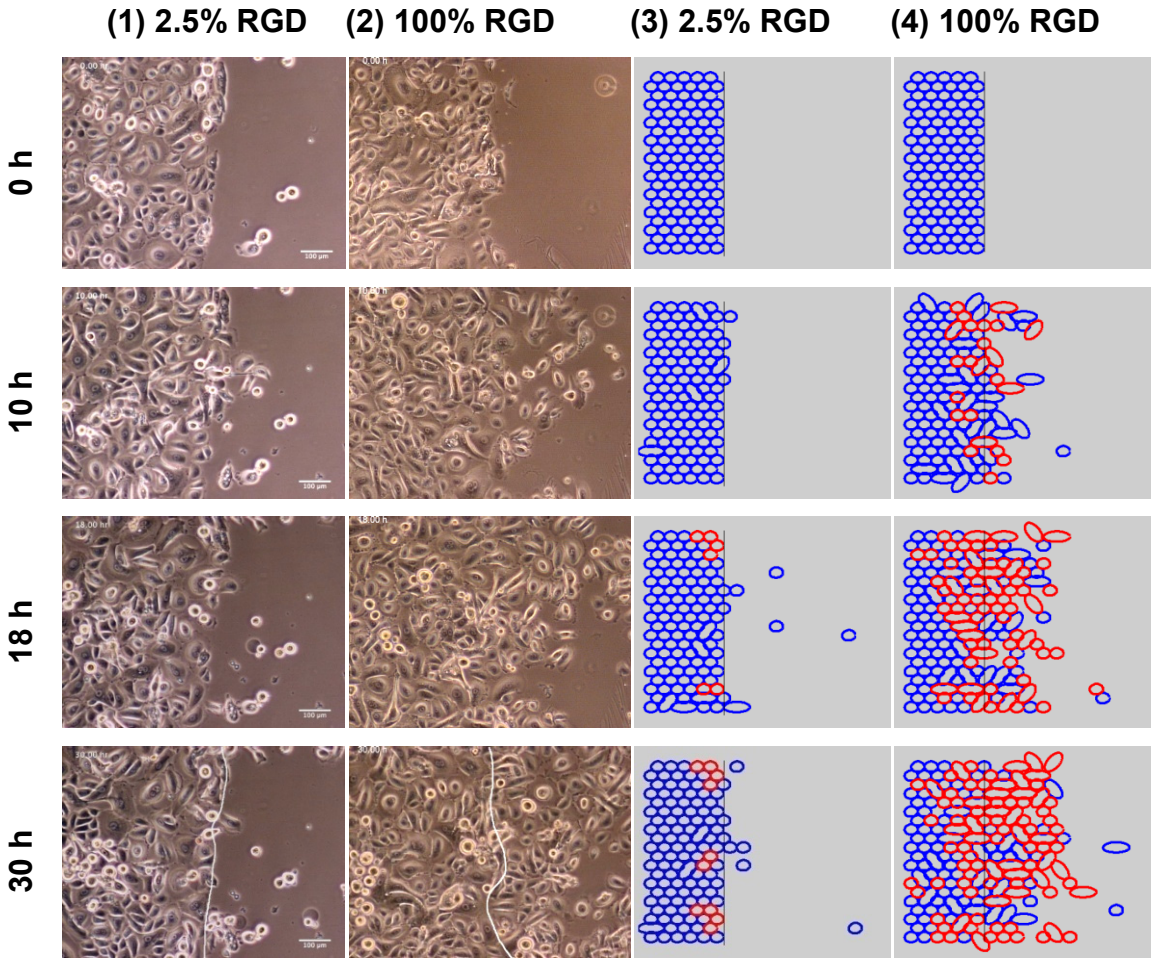
(1) 2.5% RGD
(2) 100% RGD
(3) 2.5% RGD
(4) 100% RGD
0 h
10 h
18 h
30 h

C

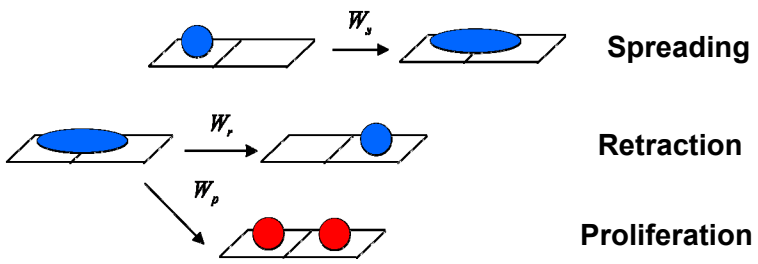
W_s
Spreading
W_r
Retraction
W_p
Proliferation

Figure 2.2 (**A)** Schematic of wound healing experiment. Cross-linked aECM proteins were spin-coated onto glass coverslips and mounted in tissue culture multi-well plates. A slab of PDMS was laid on top of the protein film and fibronectin solution was allowed to adsorb overnight at 4 ºC to aid cell attachment. HCE cells were grown to confluence and the PDMS was peeled off. The protein film was rinsed twice with serum-free media and the wounded cell sheets were allowed to migrate over the aECM protein. This process was monitored by time lapse microscopy. **(B)** Time course wound healing on 2.5% RGD and 100% RGD substrates. (Panels **1** and **2**) Experimental images showing the progression of the wound edge on 2.5% and 100% RGD, respectively, at various time intervals. (Panels **3** and **4**) Comparative snapshots of wound edges for 2.5% RGD and 100% RGD substrates. Cells that have divided are represented as red cells. The initial positions of the wound edge (i.e., the position of the interface) are indicated by white lines in the images at 30 h. (**C**) Schematic of the Monte-Carlo simulation. In the model, cells can either spread with W_s to take up two lattice sites; retract to either one of the sites with W_r or undergo proliferation with W_p.

This result was puzzling — we expected the increase in wound closure rate with RGD concentration to be a consequence of an increase in cell speed. How can the rate of wound closure increase when cell speed does not? We imagined that the critical event might be the "decision" made by each cell as it comes in contact with the test surface. Does the cell cross to the test surface or retreat to the matrix deposited beneath the confluent cell monolayer? If the rate of crossing depends on the adhesivity of the test surface, it seemed likely that wound healing should occur more rapidly on surfaces bearing higher RGD densities. In order to test this hypothesis, we performed computer simulations of the healing process.

The surface was modeled as a 2D hexagonal lattice in which each lattice site was either occupied by a cell or empty. Cell migration in the simulation proceeds via a two-step mechanism; first, the cell spreads onto an adjacent lattice site, and then it retracts to a single lattice site (Figure 2.2C). If retraction vacates the site occupied by the cell before it spread, migration has occurred.

We define the x-axis as the axis perpendicular to the wound edge, and the initial position of the wound edge (the boundary) as $x = 0$. Thus, in the initial configuration of the simulation, cells occupy all the lattice sites whose x positions are smaller than zero, and the rest of the sites are empty. As the simulation progresses, cells cross the boundary into the wound area and the value of x at the wound edge position increases.

We denote the transition probabilities for spreading, retraction, and proliferation by W_s, W_r, and W_p respectively. We use a simple model for spreading and retraction behavior to estimate the values of W_s and W_r for the different surfaces, based on experimental data (see supporting information for model details). Since FN is a major component of the matrix deposited beneath the confluent monolayer, the probabilities for spreading and retraction for lattice sites with $x < 0$ were taken to be those for FN. We estimated the proliferation rate (W_p) by constructing rate equations according to the simulation rules and solving them in the low cell concentration limit. The doubling time was then compared to experimental data. Details of the simulation scheme can be found in the supporting information of this chapter.

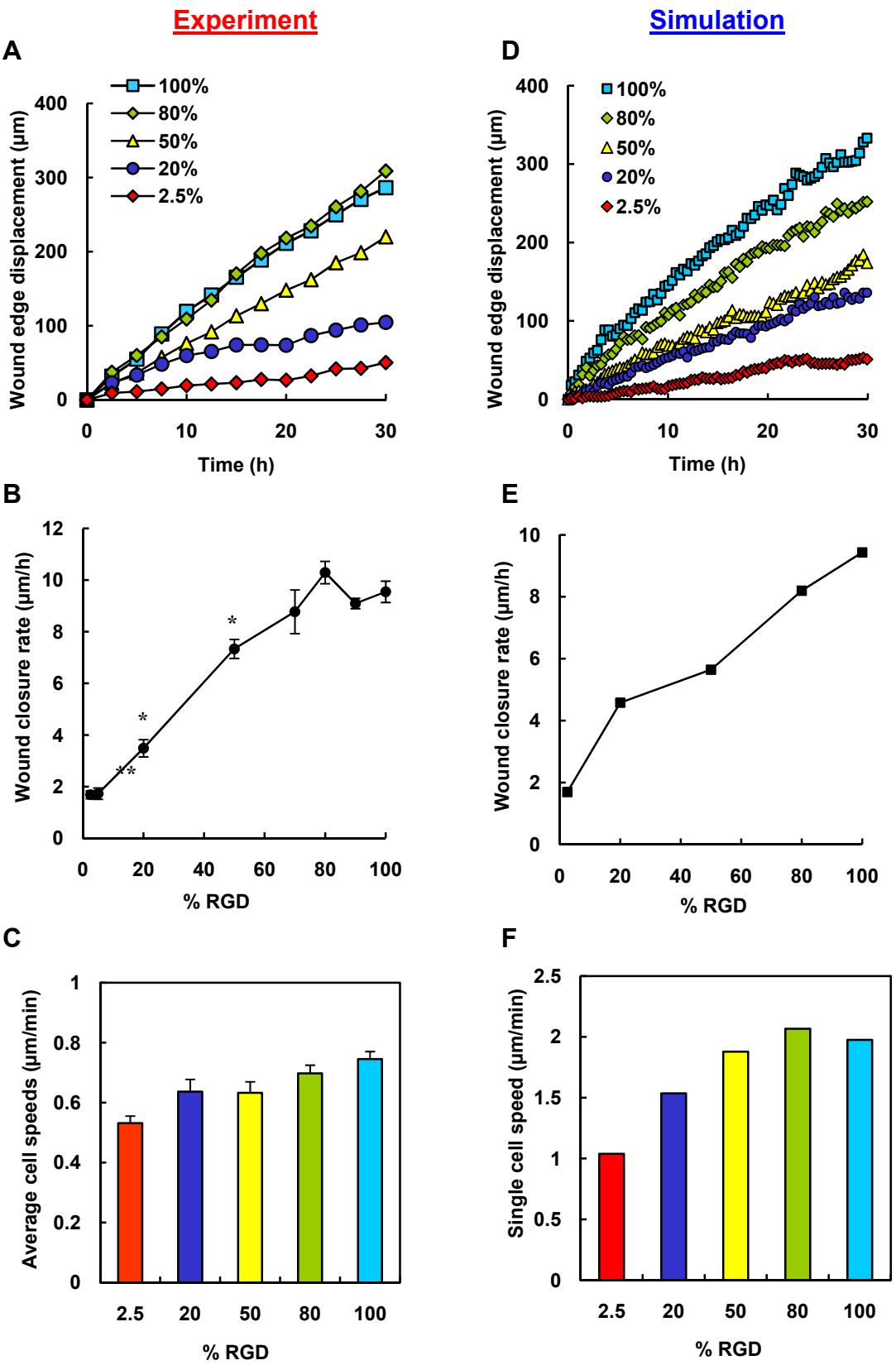
Experiment
Simulation
A
D
100%
80%
50%
20%
2.5%
Wound edge displacement (μm)
Time (h)
B
E
Wound closure rate (μm/h)
% RGD
C
F
Average cell speeds (μm/min)
Single cell speed (μm/min)
% RGD

Figure 2.3 Wound healing behavior observed in experiments (**A** to **C**) and simulations (**D** to **F**)**.** (**A**) Displacement of the wound edge for various surfaces over time. (**B**) Wound closure rate for substrates with varying RGD densities. *, significant difference from 100% RGD ($P < 0.05$). (**C**) Average cell speeds for individual cells migrating on the test surface for the last 10 h. (**D**) Displacement of simulated wound edges as a function of time. (**E**) Wound closure rate as a function of RGD percentage. The wound closure rate is five fold faster on 100% RGD than on 2.5% RGD, consistent with experimental observations. (**F**) Single cell speed as a function of RGD concentration. Only cells on the test surface were included. Error bars represent SEM.

The cells in the simulation behaved similarly to those observed experimentally, in the dynamic nature of their bonds and in the difference in cell behaviors observed on surfaces that present different densities of RGD ligands. Figure 2.2B compares snapshots taken from the simulation and from experiments for the 100% and 2.5% RGD surfaces. The wound closure rates derived from the simulation are shown in Figure 2.3E. The wound closure rate is defined as the average distance traveled by the wound edge per unit time (Figure 2.3D). As observed experimentally, there is a 5.6-fold difference between the wound closure rates on the 100% and on 2.5% RGD surfaces. Figure 2.3F shows the single cell speeds calculated from the simulation for surfaces bearing various RGD densities. At each time point, only cells on the test surface were included in the analysis. The difference between the single cell speeds on 100% RGD and 2.5% RGD is only 1.9-fold. These observations are consistent with the experimental results, and confirm that the increase in overall wound closure rate does not require faster cell migration.

The probability that a cell crosses the matrix boundary is given by its probability to spread onto the RGD test surface multiplied by its probability to retract from the FN surface, i.e., $W_s^{RGD} \times W_r^{FN}$. Hence, the ratio of the probabilities for crossing to the 100% RGD and 2.5% RGD test surfaces is: $P_{FN \to 100\%RGD} / P_{FN \to 2.5\%RGD} = W_s^{100\%RGD} / W_s^{2.5\%RGD} = 5.3$. The second equality was obtained from the spreading rates used in the simulation. As explained in detail in the supporting information, we used the cell spreading assay data (Figure 2.1E) to determine these rates. Hence, the 5.3-fold difference in crossing probability arises from the 5.3-fold difference in the rate of cell spreading. Following the same logic, we can also explain the small differences in cell speed observed on surfaces with different RGD concentrations. The ratio between single cell migration rates on 100% and 2.5% RGD is $W_s^{100\%RGD} \times W_r^{100\%RGD} / W_s^{2.5\%RGD} \times W_r^{2.5\%RGD} = 1.8$.

The simulation results suggest that the 5.6-fold variation in wound closure rates observed experimentally arises primarily from variation in boundary-crossing rates (Figure 2.5B and see supporting information, Figure A7). To measure boundary-crossing rates directly, we prepared substrates by spin-coating one layer of aECM protein on top of another (Figure 2.4). A typical surface used for studying the crossing probabilities was imaged by AFM. The height of the step at the boundary was 119.2 ± 14 nm (n = 30).

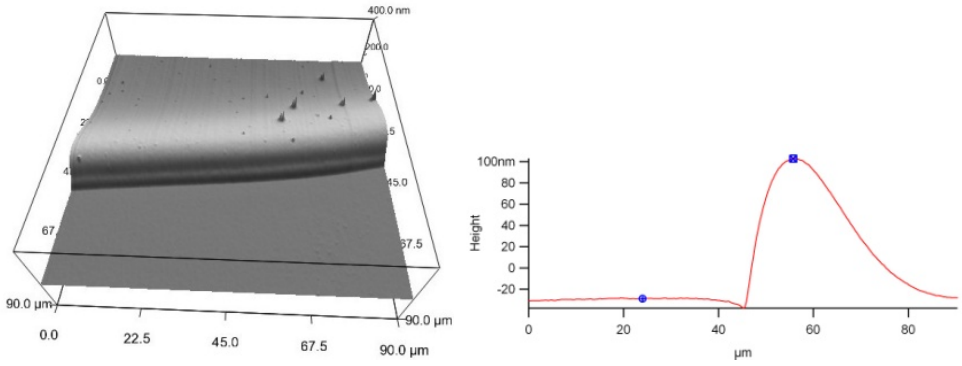

Figure 2.4 Image of typical substrate with an interface imaged using an atomic force microscope (left). A cross-section of the interface region is also shown (right).

Single HCE cells were seeded on these surfaces, and cells at the boundary were followed by time-lapse microscopy. The total time in contact with the boundary and the subsequent decision (i.e., to cross the boundary or not) were recorded for each cell. The crossing rate was calculated by dividing the number of crossings by the total time in contact with the boundary (see supporting information for crossing rate calculations). The results confirm that the crossing rate increases 5.7-fold as the adhesivity of the substrate increases (Figure 2.5C), supporting the hypothesis that the variation in wound closure rate is determined primarily by variation in the rate of boundary crossing.

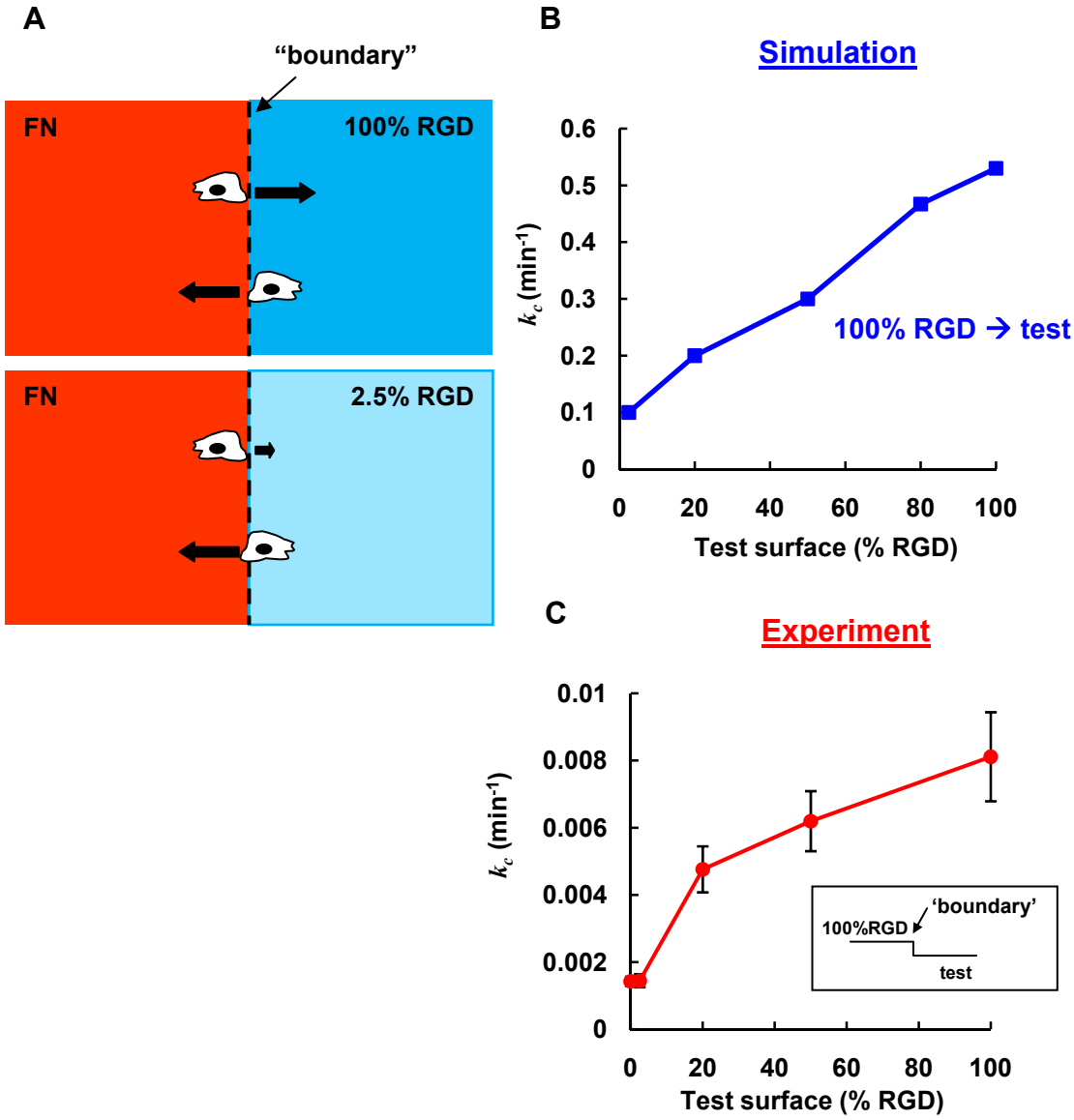

Figure 2.5 (**A**) Schematic representation of boundary crossing. Black arrows represent relative crossing rates for each condition. (**B** and **C**) show the rate constants of crossing, k_c (from 100% RGD to the test surfaces) for simulation and experimental data, respectively. In both curves, the crossing rates from 100% RGD to 100% RGD and from 100% RGD to 2.5% RGD differ by a factor of five. Error bars in **C** are experimental errors (see supporting information for this chapter).

2.4 Conclusions

In summary, we find that the rate of healing of epithelial cell monolayers cultured on aECM proteins increases with increasing density of adhesion ligands presented at the substrate surface. As shown both experimentally and through simulation of the healing process, the variation in healing rate arises not from variation in the rate of cell migration, but instead from variation in the rate at which cells cross the boundary between the matrix deposited by the cell monolayer and the aECM protein. The simulation method described here can be applied to many cell types, and — through variation in the cell-cell interaction energy (see supporting information) — captures a broad range of wound healing behavior, from diffusion-like behavior in which cell-cell contacts break and reform (as observed for corneal epithelial cells) to behavior that resembles that of an elastic sheet in which cell-cell contacts remain unchanged during wound healing (as observed in monolayers of MDCK cells (*27*)).

2.5 Acknowledgements

We acknowledge Drs. Julie Liu, Paul Nowatzki, and Stacey Maskarinec for help with protein expression and cell culture. We also thank Dr. Zhen-Gang Wang for useful advice on the simulation model. E.F. is supported by the Nanyang Overseas Scholarship, Singapore; S.T. is supported by the Human Frontier Science Program Cross-Disciplinary Fellowship. This work is funded by the NSF Center for the Science and Engineering at Caltech and by NIH grant EB1971.

2.6 References

1. P. Martin, J. Lewis, *Science* **360**, 179 (1992).

2. W. M. Bement, P. Forscher, M. S. Mooseker, *J. Cell. Biol.* **121**, 565 (1993).

3. P. J. Sammak, L. E. Hinman, P. O. T. Tran, M. D. Sjaastad, T. E. Machen, *J. Cell Sci.* **110**, 465 (1997).

4. M. Poujade et al., *Proc. Natl. Acad. Sci. U.S.A.* **104**, 15988 (2007).

5. E. R. Block, A. R. Matela, N. SundarRaj, E. R. Iszkula,J. K. Klarlund, *J. Biol. Chem.* **279**, 24307 (2004).

6. D. L. Nikolic, A. N. Boettiger, D. Bar-Sagi, J. D. Carbeck, S. Y. Shvartsman, *Am. J Physiol. Cell Physiol.* **291**, 68 (2005).

7. G. J. Todaro, G. K. Lazar, H. Green, *J. Cell Physiol.* **66**, 325 (1965).

8. K. Suzuki, J. Saito, R. Yanai, N. Yamada, T. Chikama, K. Seki, T. Nishida, *Prog. Ret. Eye Res.* **22**, 113 (2003).

9. R. A. F. Clark, *J. Invest. Dermatol.* **94**, 128S (1990).

10. S. P. Palecek, J. C. Loftus, M. H. Ginsberg, D. A. Lauffenburger, A. F. Horwitz, *Nature* **385**, 537 (1997).

11. D. K. Pettit, A. S. Hoffman, T. A. Horbett, *J. Biomed. Mater. Res.* **28**, 685 (1994).

12. R. van Horssen, N. Galjart, J. A. P. Rens, A. M. M. Eggermont, T. L. M. ten Hagen, *J. Cell Biochem.* **99**, 1536 (2006).

13. L. Aucoin, C. M. Griffith, G. Pleizier,Y. Deslandes, H. Sheardown, *J. Biomater. Sci. Polymer Edn.* **13**, 447 (2002).

14. P. J. Nowatzki, D. A. Tirrell, *Biomaterials*, 1261 (2003).

15. K. Di Zio, D. A. Tirrell, *Macromolecules* **36**, 1553 (2003).

16. J. C. Liu, S. C. Heilshorn, D. A. Tirrell, *Biomacromolecules* **5**, 497 (2003).

17. S. C. Heilshorn, K. A. Di Zio, E. R. Welsh, D. A. Tirrell, *Biomaterials* **24**, 4245 (2003).

18. J. C. Liu, D. A. Tirrell, *Biomacromolecules* **9**, 2984 (2008).

19. L. Luo, P. S. Reinach, W. W. Y. Kao, *Exp. Biol. Med. Vol.* **226**, 653 (2001).

20. M. A. Stepp, *Exp. Eye Res.* **83**, 3 (2006).

21. E. K. Dimitriadis, F. Horkay, J. Maresca, B. Kachar, R. S. Chadwick, *Biophys. J.* **82**, 2798 (2002).

22. M. Zhao, B. Song, J. Pu, J. V. Forrester, C. D. McCaig, *FASEB J.* **17**, 397 (2003).

23. M. D. M. Evans, J. G. Steele, *J. Biomed. Mater. Res.* **40**, 621 (1997).

24. M. D. M. Evans, J. G. Steele, *Exp. Cell Res.* **233**, 88 (1997).

25. K. Y. Chan, D. L. Patton, Y. T. Cosgrove, *Invest. Opthalmol. Vis. Sci.* **30**, 2488 (1989).

26. R. Farooqui, G. Fenteany, *J. Cell Sci.* **118**, 51 (2005).

ADDITIONAL INFORMATION FOR CHAPTER 2

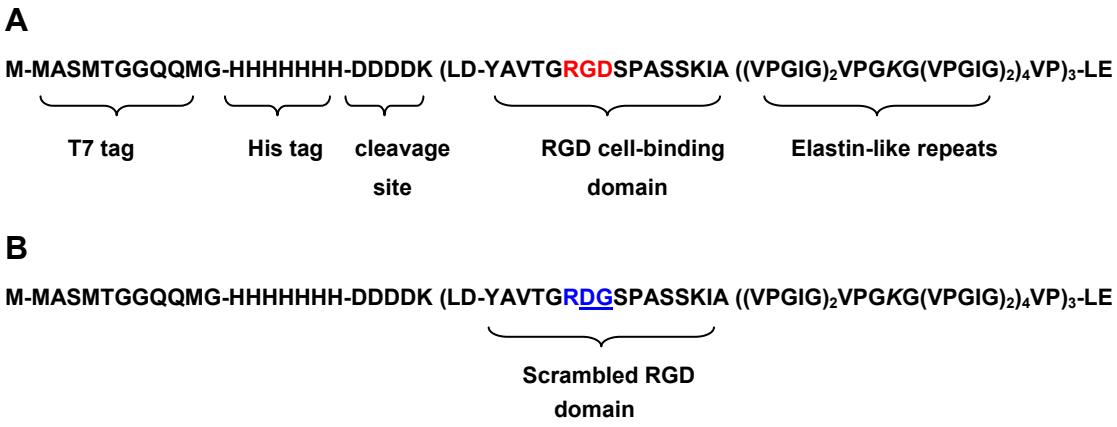

Figure A1. Amino acid sequences of aECM proteins containing (A) RGD and (B) RDG cell-binding domains. Each aECM protein contained a T7 tag, a hexahistidine tag, an enterokinase cleavage site, and elastin-like domains containing lysine residues (italicized) for crosslinking.

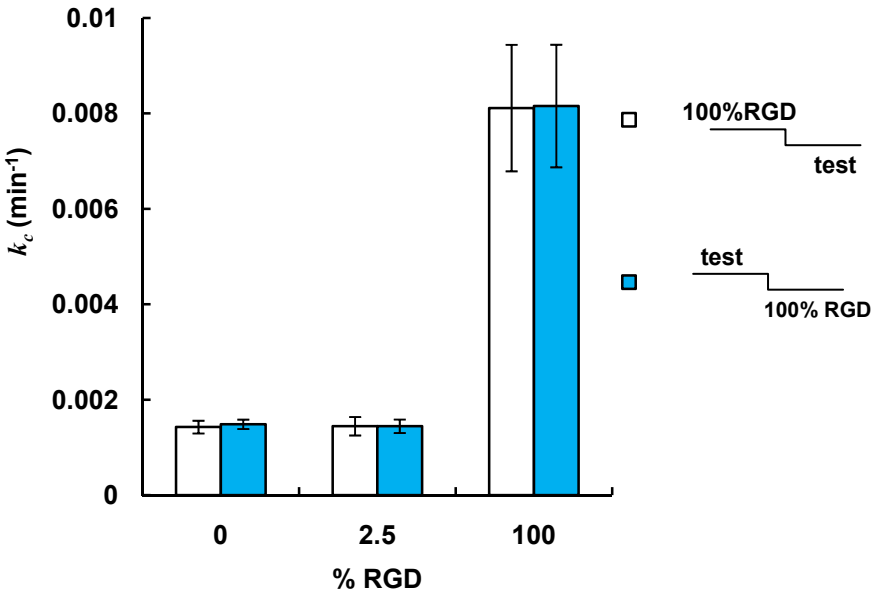

Figure A2. Rate constants of interface crossing, k_c from 100% RGD into various test surfaces. The crossing probabilities computed for both configurations of the interface. There were no significant differences between the rate constants for the two configurations of each test surface, suggesting that the small "step" at the interface did not affect the boundary-crossing rate.

Mathematical model

A simple model for spreading and retraction

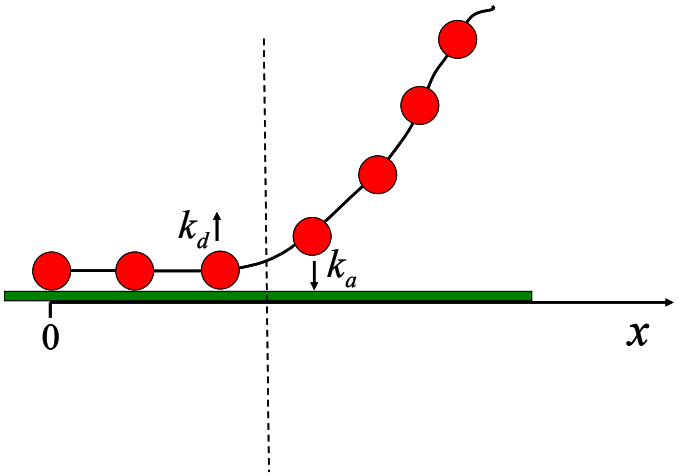

Figure A3. A schematic illustration of the cell spreading and retraction model. The beads represent integrin receptor clusters, while the chain represents the cell membrane. The cell edge is represented by the dashed line. Receptor clusters adjacent to the cell edge can adsorb or desorb with rate constants k_a and k_d respectively.

We use a simplified picture for cell spreading and retraction in order to estimate numerical values for the speed of these processes. In Fig. A3, the cell membrane is modeled as a chain of beads which represent integrin receptors or clusters. Both spreading and retraction advance through adsorption and desorption of receptor clusters at the ligand-bearing surface. Only the receptor clusters adjacent to the cell edge (represented by the dashed line in Fig. A3) can adsorb or desorb. The rate constants for adsorption and desorption are k_a and k_d, respectively.

During spreading and retraction, the cell edge performs a random walk where each adsorption event results in an increase in its *x* position while each desorption event results in a decrease in its *x* position.

The master equation, describing the processes discussed above, is of the form:

(1) $$\frac{dP(x,t)}{dt} = k_a P(x-1,t) + k_d P(x+1,t) - (k_a + k_d) P(x,t)$$

where $P(x,t)$ is the probability of the cell edge to be at position *x* at time *t*, and *x* is measured in units equal to the average distance between receptor clusters.

The solution for the average cell edge displacement is:

(2) $$< x >= (k_a - k_d) \cdot t$$

An increase in $< x >$ corresponds to an increase in the cell area in contact with the surface. Therefore, we define the spreading rate, W_s, as the change in the average value of *x* with time:

(3) $$W_s = \frac{d\langle x \rangle}{dt} = (k_a^s - k_d^s)$$

Similarly, the retraction rate, W_r, is defined as:

(4) $$W_r = -\frac{d\langle x \rangle}{dt} = (k_d^r - k_a^r)$$

The forces exerted by the cell influence the effective rate of receptor adsorption and desorption events (k_a and k_d). Since, the forces exerted by the cell are different when the

cell is in a state of spreading or retraction, the rate constants for adsorption and desorption in these two cases will be different. Consequently, we add a superscript in Equations 3 and 4 (*s* or *r*) to denote the cell state (spreading or retraction).

In a cell-free system with receptors incorporated in a rigid planar membrane, the binding of the receptors to the surface ligands, can be described as a second order reaction. Denoting the rate constant for binding by k and the rate constant for unbinding by k_{-1}, the ratio between these rate constants is: $k_{-1}/k = \exp(-\varepsilon / k_B T)$ where $\varepsilon > 0$ is the binding energy (the difference in energy between the unbound and bound states).

For the case of a flexible membrane, the spreading process is associated with a change in membrane shape. The shape deformation results in an energy barrier which we denote by ε_{el}.

Spreading and retraction processes are not spontaneous and require forces to be applied by the cell (*1*). In the case of spreading, a protrusive force is exerted on the cell membrane, thereby reducing the energy barrier associated with membrane deformation in an amount $f\gamma$ where *f* is the force applied by the cell and γ is the length along which the force is applied (*2, 3*). In this case the rate constants for adsorption and desorption in our model are:

(5) $$k_a^s = k\exp(-\varepsilon_{el}/k_B T + f\gamma / k_B T), \quad k_d^s = k\exp(-\varepsilon / k_B T)$$

When retracting, the cell pulls on the receptor-ligand bond, thereby reducing the energy barrier associated with bond breakage in an amount $f'\gamma'$ (*1, 2*).

In this case, the rate constants take the form:

(6) $k_a^r = k\exp(-\varepsilon_{el}/k_BT), \quad k_d^r = k\exp(-\varepsilon/k_BT + f'\gamma'/k_BT)$

Following Equations 3 - 6, the rates for spreading and retraction can be expressed as:

(7) $$W_s = k\exp(-\varepsilon_{el}/k_BT + f\gamma/k_BT) - k\exp(-\varepsilon/k_BT)$$

(8) $$W_r = k\exp(-\varepsilon/k_BT + f'\gamma'/k_BT) - k\exp(-\varepsilon_{el}/k_BT)$$

Using equations 7 - 8, we can connect between the spreading and retraction rates on surfaces with the same RGD fraction, φ_{RGD} :

(9) $$\tilde{W}_r(\varphi_{RGD}) = \exp(f'\gamma'/k_BT)\left[A - \tilde{W}_s(\varphi_{RGD})\right] - k\exp(-\varepsilon_{el}/k_BT)/W_s(FN)$$

In Equation 9, $W_s(FN)$ denotes the spreading rate on fibronectin, $\tilde{W}_s(\varphi_{RGD}) = W_s(\varphi_{RGD})/W_s(FN)$ and $\tilde{W}_r(\varphi_{RGD}) = W_r(\varphi_{RGD})/W_s(FN)$ are the spreading and retraction rates relative to the spreading rate on fibronectin and $A \equiv k\exp(-\varepsilon_{el}/k_BT + f\gamma/k_BT)/W_s(FN)$.

We can use the results from the spreading assay (Fig. 2.1E) in order to get a numerical value for the constant *A*. If we assume that the binding energy, ε is proportional to the RGD fraction on the surface, i.e., $\varepsilon = \tilde{\varepsilon}\varphi_{RGD}$, we get

(10) $$\tilde{W}_s = A - B\exp\left(-\tilde{\varepsilon}\varphi_{RGD} / k_B T\right)$$

where $B \equiv k/W_s(FN)$.

The percent spread cells on aECM with different RGD concentrations after 4 h (shown in Fig. 2.1E) relative to the percent of spread cells on FN after 4 h, was taken as a measure for the relative rate of cell spreading, $\tilde{W}_s$, and was fitted to Equation 10. The fit is shown in Fig. A4.

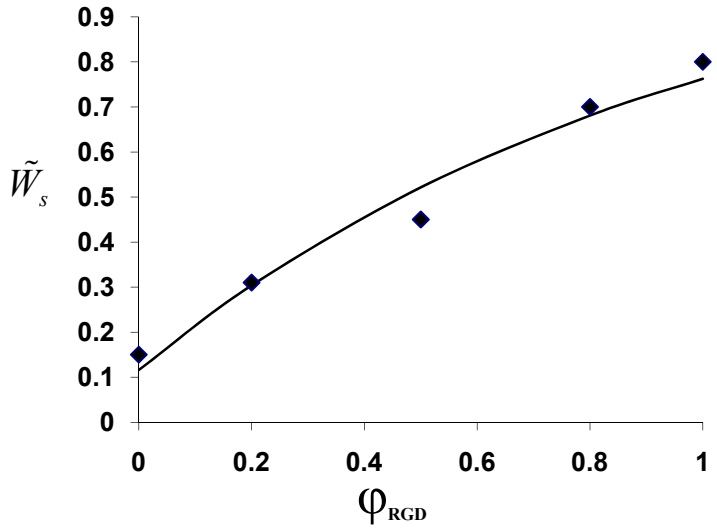

Figure A4. The fit of the experimental spreading data to the theoretical expression for the relative spreading rate, Equation 10.

Out of the fit we obtain $A = 1.11$

The rest of the model parameters were estimated on the basis of experimental results described in the literature:

1. γ is the characteristic distance between bonds between the cell and the substrate (the distance between beads in our model) and is estimated to be 100 nm (*4*).

2. The characteristic traction force is assumed in the literature to be on the order of 1 nN/μm^2 (*3, 5, 6*) and the protrusion has a typical diameter of 0.1 μm (*6*), comparable to the average distance between bonds (*4*). These estimates lead to a traction force, f', on the order of 8 pN. The RGD-integrin bond length, γ', is on the order of 1 nm (*2, 3*).

3. Recent estimates suggest that the thermal deformation of the membrane is on the order of 5-10 nm (*6, 7*) implying that the energy required for deformation on the scale of the distance between bonds (~100 nm) cannot be provided by thermal fluctuations. Consequently, we assume that the term $\exp(-\varepsilon_{el} / k_B T)$ in Equation 9 is negligible.

The rates of spreading and retraction in the simulation are measured in units of the spreading on FN, i.e., the values used in the simulation are $\tilde{W}_s$ and $\tilde{W}_r$ respectively. Notice that in these units, $\tilde{W}_s(FN) = W_s(FN) / W_s(FN) = 1$. For each RGD concentration, φ_{RGD}, the spreading rate, $\tilde{W}_s(\varphi_{RGD})$ was taken from the experimental data presented in

Fig. A4. The value for the retraction rate on the same surface, $\tilde{W}_r(\varphi_{RGD})$ was calculated using Equation 9.

Estimation of the proliferation rate

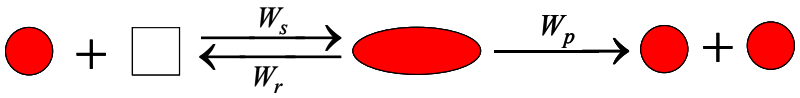

Figure A5. An illustration of the proliferation kinetic scheme. The white box represents an empty neighboring lattice site on which the cell can spread in order to proliferate.

The number of cells confined to a single lattice site is denoted by n_1 ( ); the number of spread on two adjacent lattice sites by: n_2( ). The empty square in Fig. A5 represents an empty neighboring site on the lattice. The rates for spreading, retraction and proliferation steps are denoted by W_s ,W_r and W_p respectively.

In our model, only cells that are spread on two adjacent lattice sites can proliferate. This assumption is consistent with the observation that decreased cell spreading can inhibit proliferation signals (*8*), and it creates an effective time lag between consecutive cell divisions, resembling inter-phase *(9)*.

The rate equations for the kinetic scheme illustrated in Fig. A5 are:

(10) $$\frac{dn_1}{dt} = -W_s n_1 (1 - n_1 / n_1^* - n_2 / n_2^*) + W_r n_2 + 2W_p n_2$$

(11) $$\frac{dn_2}{dt} = W_s n_1 (1 - n_1 / n_1^* - n_2 / n_2^*) - W_r n_2 - W_p n_2$$

The first term is the rate of spreading, where the probability to find a neighboring empty lattice site is taken to be the mean field probability, i.e., $P_{empty\_site} = (1 - \theta)$ where θ is the fraction of occupied sites on the lattice and is given by $\theta = n_1 / n_1^* + n_2 / n_2^*$ where n_1^* is the number of cells that occupy a single site when at confluence. Likewise, n_2^* is the number of cells that occupy two adjacent sites at confluence.

The change in the total number of cells $n = n_1 + n_2$ is then:

(12) $$\frac{dn}{dt} = \frac{dn_1}{dt} + \frac{dn_2}{dt} = W_p n_2$$

Since for most cases, $W_p << W_r, W_s$, we can assume fast equilibrium in order to solve the rate equations (Equations 10 - 12). In the limit of low cell concentration ($n_1 / n_1^* << 1$), we get the expected exponential growth:

(13) $$\frac{dn}{dt} = \frac{W_p}{1 + \left(\frac{W_r}{W_s} \right)} n$$

The doubling time, t_D, for a cell population which grows according to the kinetic scheme presented in Fig. A5 is:

(13) $$t_D = \frac{\ln 2}{W_p}\left(1 + W_r / W_s\right)$$

According to the literature, the doubling time for human corneal epithelial (HCE) cells is estimated to be 25 h (*10*). Using the values for W_r and W_s on FN, we get $W_p = 0.05h^{-1}$. We assume that W_p is identical on all the surfaces.

Simulation details

We use a dynamic Monte Carlo scheme (*11, 12*) to simulate the dynamics of collective cell migration. The surface is modeled as 100×100 hexagonal lattice with a lattice constant of d = 50 μm, which is on the order of a cell diameter. At time t = 0, the first 10 columns of the lattice are occupied by cells (total number of cells, N = 1000), while the rest of the lattice sites are empty. Since proliferation is enabled, N increases with time.

In every Monte Carlo step, N cells are chosen randomly and an attempt is made to change their state according to the appropriate probabilities. As explained before, the spreading rate on fibronectin (FN) in the simulation is defined as 1 and the rest of the rates are calibrated accordingly. All the rates in the simulation are scaled to make sure that the time steps are small enough so that in any Monte-Carlo (MC) step only one event can occur. The conversion between simulation time and experimental time was done by a one-time calibration, equating the wound closure rate for the case of 2.5% RGD obtained from the simulation and from the experiment. Working backwards we get: 1 MC step equals 0.15 min and $W_s(FN) = 0.54$ min^{-1}.

Cell-cell interactions

Wound healing behavior depends not only on cell-aECM interaction but also on the inter-cellular interaction. The energy of a cell fluctuates, but unlike in a fluid, the origin of the fluctuations is not collisions with the solvent or the thermal energy. The fluctuations in energy in a cellular system originate from fluctuations around the steady state of the biochemical networks of the cell (*13*). Consequently, it is accepted to define an effective temperature $T_{eff} = F_T / k_B$ where F_T is the magnitude of the energy fluctuations and k_B is the Boltzmann constant (*14-16*). As a result, the probability of a cell to have an energy fluctuation ε' is $\exp(-\varepsilon' / F_T)$.

In the simulation, we measure the intercellular interaction energy, $\varepsilon_{cell-cell}$, in units of F_T and use a value of $\varepsilon_{cell-cell} / F_T = 1.0$. The interaction energy between cells comes into play in the simulation for the case of cell retraction. When a cell retracts, there is an active force that pulls it from the surface and from its neighbors as explained in the model for spreading and retraction (see section of model for spreading and retraction). This force can either lead to cell-cell bond breakage or to retraction of the cell, pulling the neighboring cell along.

Let us denote the number of neighbors that the cell in question would lose upon retraction by υ. The cell can retract and break the bonds with its neighbors with probability $W_r \times \left(\exp(-\varepsilon_{cell-cell} / F_T)\right)^{\upsilon}$. Or the cell can retract, break the bonds with υ-1 of its neighbors and pull the remaining cells with it with probability $W_r \times \left(\exp(-\varepsilon_{cell-cell} / F_T)\right)^{\upsilon-1}$.

A neighboring cell can only be stretched if it occupies a single lattice site. This is to ensure that the total elastic energy of the cell does not exceed the cell fluctuation energy F_T.

Single cell crossing rates

When a cell is at the interface, it can either cross the interface with a rate constant, k_c or move away from the interface with a rate constant, k_b as illustrated in the schematic figure below.

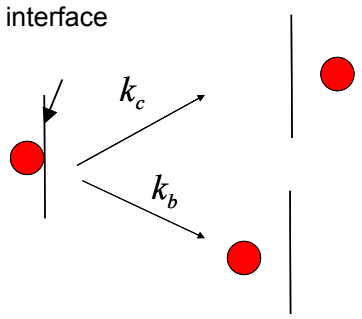

Figure A6. Schematic diagram of cell at an interface, showing two possible outcomes. A cell can cross the interface with a rate constant k_c, or it can move away with a rate constant, k_b.

From the time-lapse movies, we recorded the time spent by the cell at the interface until a reaction occurs (i.e., waiting time), as well as the outcome (i.e. crossing or moving away). In order to extract the rate constant for interface crossing from the experiment, it is necessary to know the waiting time distribution for cells at the interface.

Let us define $P_0(t;t_0)$ as the probability that no event occurs in the interval (t_0, t_0+t) and assume that the events are independent and the rate constants do not depend on time.

Then, $P_0(t+dt;t_0) = P_0(t;t_0) \times \left(1 - \sum_i k_i dt\right)$, where k_i is the rate constant for event i (in our case: $i = c, b$).

Consequently, $\frac{P_0(t+dt;t_0) - P_0(t;t_0)}{dt} = \left(-\sum_i k_i\right) P_0(t;t_0)$

And in the limit of $dt \to 0$, we get:

$\frac{dP_0(t)}{dt} = \left(-\sum_i k_i\right) P_0(t)$ so that $P_0(t) = \exp\left(-\sum_i k_i \times t\right)$

We denote the waiting time distribution as $w(t)$. The waiting time distribution can be expressed as:

$$w(t) = \frac{P_0(t) - P_0(t+dt)}{dt} = -\frac{d}{dt} P_0(t)$$

and hence,

(14) $$w(t) = K \exp(-Kt)$$

where $K = \sum_i k_i$ is the sum of the rate constants for all possible events.

Using the waiting time distribution (Equation 14), the average waiting time is:

(15) $$\langle t \rangle = \frac{\int_0^\infty t \times K \exp(-Kt)\, dt}{\int_0^\infty K \exp(-Kt)\, dt} = \frac{1}{K}$$

In the case of the cell crossing experiment, the waiting at the interface can end with either crossing of the interface (k_c) or with bouncing back (k_b) and thus, $\langle t \rangle = 1/(k_c + k_b)$.

If we define N_1 as the number of events which end with interface crossing and *N* as the total number of events, we get:

(16) $$\frac{N_c}{N} = \frac{k_c}{k_c + k_b}$$

Using Equations 14-16, the rate constant of interface crossing can be expressed as:

(17) $$k_c = \frac{N_c}{N \langle t \rangle}$$

Notice, that according to Equation 17, the rate constant of interface crossing, k_c can be calculated as the number of crossing events divided by the total waiting time at the interface.

The 15-min time interval between two consecutive time-lapse images is taken to be the experimental error for the waiting time.

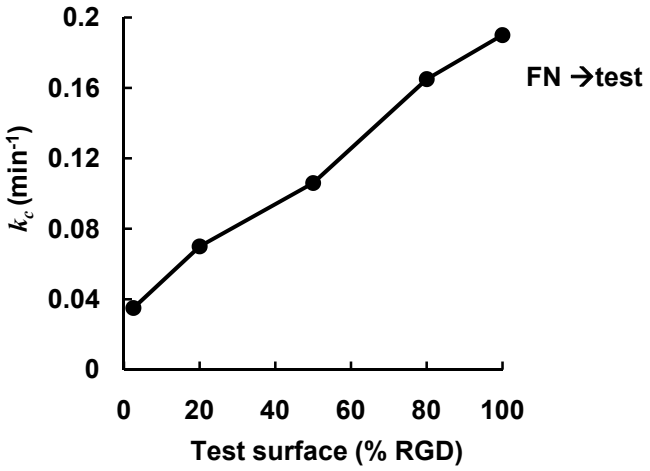

Figure A7. The rate constants of interface crossing from FN to test surfaces obtained from simulation. The ratio between crossing rates from 100% RGD to 100% RGD and 100% RGD to 2.5% RGD is also five fold, consistent with experimental observations (Table A1).

	Simulation	Experiment
Surface composition (the line represents the wound edge at time t=0)	**FN|RGD**	**FN|RGD**
Wound closure rate (μm/h) (100% RGD)	9.4	9.6
Wound closure rate (μm/h) (2.5% RGD)	1.7	1.7
Wound closure rate ratio (100% RGD/2.5% RGD)	5.6	5.6
Single cell speed ratio (100% RGD/2.5% RGD)	1.9	1.4
$P_{FN \to RGD}$ ratio (100% RGD/2.5% RGD)	4.7	5.7

Table A1. Summary of the rates for 100% and 2.5% RGD surfaces.

References

1. D. A. Lauffenburger, *Cell* **84**, 359 (1996).

2. G. I. Bell, *Science* **200**, 618 (1978).

3. S. P. Palecek, A. F. Horwitz, D. A. Lauffenburger, *Ann. Biomed. Eng.* **27**, 219 (1999).

4. T. R. Weikl, M. Asfaw, H. Krobath, B. Rozycki, R. Lipowsky, *Soft Matter* **5**, 3213 (2009).

5. M. Prass, K. Jacobson, A. Mogilner, M. Radmacher, *J. Cell Biol.* **174**, 767 (2006).

6. A. Pierres, V. Monnet-Corti, A. M. Benoliel, P. Bongrand, *Trends in Cell Biol.* **19**, 428 (2009).

7. A. Zidovska, E. Sackmann, *Phys. Rev. Lett.* **96**, 048103 (2006).

8. C. M. Nelson, C. S. Chen, *FEBS Lett.* **514**, 238 (2002).

9. B. Alberts et al., *Molecular Biology of the Cell*. (Garland Science, 2008), pp. 637-655.

10. C. R. Kahn, E. Young, I. H. Lee, J. S. Rhim, *Invest. Opthalmol. Vis. Sci.* **34**, 3429 (1993).

11. K. A. Fichthorn, W. H. Weinberg, *J. Chem. Phys.* **95**, 1090 (1991).

12. C. H. Kang, W. H. Weinberg, *Accts. Chem. Res.* **25**, 253 (1992).

13. B. C. Goodwin, *Temporal Organization in Cells: A Dynamic Theory of Cellular Control Processes*. (Academic Press, 1963), pp. 55-80.

14. D. A. Beysens, G. Forgacs, J. A. Glazier, *Proc. Natl. Acad. Sci. U.S.A.* **97**, 9467 (2000).

15. A. Neagu, K. Jakab, R. Jamison, G. Forgacs, *Phys. Rev. Lett.* **95**, 178104 (2005).

16. D. Drasdo, S. Hohme, *Phys. Biol.* **2**, 133 (2005).